Source parameters of the $M_W = 6.1$ 1910 Adra earthquake (southern Spain)

Daniel Stich,[1] Josep Batlló,[2,*] Jose Morales,[1] Ramon Macià[3,4] and Savka Dineva[5]

[1]*Instituto Andaluz de Geofísica, Universidad de Granada, Observatorio de Cartuja, Campus Universitario de Cartuja s/n,* 18071 *Granada, Spain.*
E-mail: daniel@iag.ugr.es
[2]*Department Matemática Aplicada I. Universitat Politècnica de Catalunya*
[3]*Department Matemática Aplicada II. Universitat Politècnica de Catalunya*
[4]*Laboratori d'Estudis Geofísics Eduard Fontsere. Institut d'Estudis Catalans*
[5]*Department of Earth Sciences. University of Western Ontario*

SUMMARY

We examine and model analogue recordings from 6 early mechanical seismographs for the 1910 June 16 earthquake at Adra, Southern Spain. Modern standard, time-domain analysis techniques were applied to the historical data to estimate the source parameters of the event:

The regional sparse network data were inverted for the deviatoric seismic moment tensor. The best moment tensor solution corresponds to a $M_0 = 1.50 \cdot 10^{18}$ Nm, M_W 6.1 oblique strike-slip event at 16 km depth. Our preferred faulting solution is: strike 122°, dip 80°, rake −137°, in very good agreement with available neo- and seismotectonic data. The source time function of this earthquake was estimated by deconvolving recordings of a M_W 5.5 aftershock that occurred the same day. The time function indicates a total rupture time of 4.5 s, corresponding to estimates for mainshock rupture length of 12 km, and stress drop of 29 bar.

Key words: historical seismograms, moment tensor inversion, source time function, waveform modelling.

INTRODUCTION

By the beginning of the 20th century, seismometer technology had advanced towards typical observing stations with 2-component, intermediate-period, horizontal instruments, transferring earth motion continuously onto smoked paper. Then, soon after 1900, a number of new seismological observatories began recording and investigating earthquakes in various European countries, forming an early but very sparse and heterogeneous European seismic network. Near the end of that decade, on 1910 June 16, the area around the small town of Adra, southern Spain, was struck by a magnitude 6 earthquake, recorded at the five operating Spanish stations and many foreign observatories. Though several larger or comparable events did occur on the Iberian Peninsula in pre-instrumental times, the 1910 Adra event is still the largest instrumentally-recorded crustal earthquake in Spain. Its magnitude was surpassed only by the 1954 deep focus event beneath Granada ($m_b = 7.1$, $M_w = 7.8$, Chung & Kanamori 1976). The source parameters of this earthquake are of considerable interest for regional seismotectonics and seismic hazard assessment. A second motivation for this study was to learn what information can be gathered from these historical recordings.

The mainshock occurred on 1910 June 16, 4:16 UTC and caused destruction corresponding to macroseismic intensity I_0 = VIII MSK

in Adra on the southern coast of Spain (Vidal 1986). It was felt with I_0 = VI in the cities of Almeria, Granada and Malaga, about 50 to 100 km from the epicentre. The earthquake was reportedly also noticed offshore Adra on a steamboat and on fishing boats (macroseismic observations in Sanchez Navarro-Neumann (1911). A body wave magnitude of $m_b = 6.3$ (Karnik 1969) and a surface wave magnitude of $M_S = 6.1$ (Gutenberg & Richter 1954) have been assigned to this event. Macroseismic and instrumental data indicate an epicentre offshore in the Alboran Sea. Based on the available phase readings, epicentres were computed about 5 km from Adra (36.7°N, 3.1°W, Karnik 1969), about 15 km from Adra (36.58°N, 3.08°W, Vidal 1986), as well as far westward (36.5°N, 4°W, Gutenberg & Richter 1954). However, the latter is inconsistent with the macroseismic observations. On June 16, thirty-seven aftershocks were been detected at Cartuja seismic observatory in Granada, sixteen of them felt by the population. A major aftershock of magnitude $m_b = 5.5$ occurred at 16:27 UTC (Karnik 1969), causing destruction corresponding to I_0 = VII and affecting mainly those constructions that had already been damaged by the mainshock (Sanchez Navarro-Neumann 1911).

For this study we digitized historical data of the mainshock and the major aftershock, and applied two standard time domain analysis techniques of modern seismology to them. A full deviatoric moment tensor inversion yields the source mechanism of the main event and its total seismic moment. The deconvolution of aftershock

★Now at: Observatori de l'Ebre, CSIC-URL, Roquetes.

recordings from the main event yields the relative source time function and leads to an estimate of rupture duration, fault plane dimension and dynamic stress drop for the major event as well as seismic moment for the aftershock. Data quality and azimuthal coverage are challenging for these earthquakes and we perform systematic forward modelling of alternative solutions as a resolution test for the inverted faulting mechanism. Finally the mechanism of the 1910 Adra event is compared to recent regional moment tensor solutions and correlated with available local neotectonic and seismotectonic data to identify the active fault plane.

MAINSHOCK DATA

We were able to recover recordings of the 1910 Adra mainshock at six instruments in Spain, the Netherlands and Italy, and recordings of the major aftershock at four instruments in Spain and the Netherlands. These include the Bosch-Omori seismographs at Toledo Observatory (TOL), central Spain, the Grablovitz seismographs at Ebro Observatory (EBR), north-eastern Spain, and at Porto d'Ischia Observatory (PDI), Italy, the Stiattesi seismograph at the 'Collegio alla Querce' Observatory (FIR), Florence, Italy, and both Wiechert and Bosch-Omori instruments at De Bilt Observatory (DBN), Utrecht, the Netherlands (Fig. 1).

Obtaining the reliable digitized seismogram sections for recordings at the beginning of the 20th century is not a straightforward procedure. However, our previous experience (Dineva *et al.* 2002; Batlló *et al.* 1997) has been of great assistance. The data restoration, that is the sequence from paper recording to digitized data, was accomplished in four steps: (a) Seismogram scanning: As grey scale images with a resolution of 600–1200 dpi. (b) Digitizing: The quality of smoked paper records is not suitable for any of the automatic digitizing programs available. Consequently, the records were digitized manually with a programme providing digitized ASCII points from the raster images. (c) Correction for record curvature and uneven speed: We used the same formulae as those found in Grabrovec & Allegretti (1994) and Samardjieva *et al.* (1997). (d) Interpolation: The data were smoothed using linear interpolation to obtain an equal sampling interval of 0.1 s.
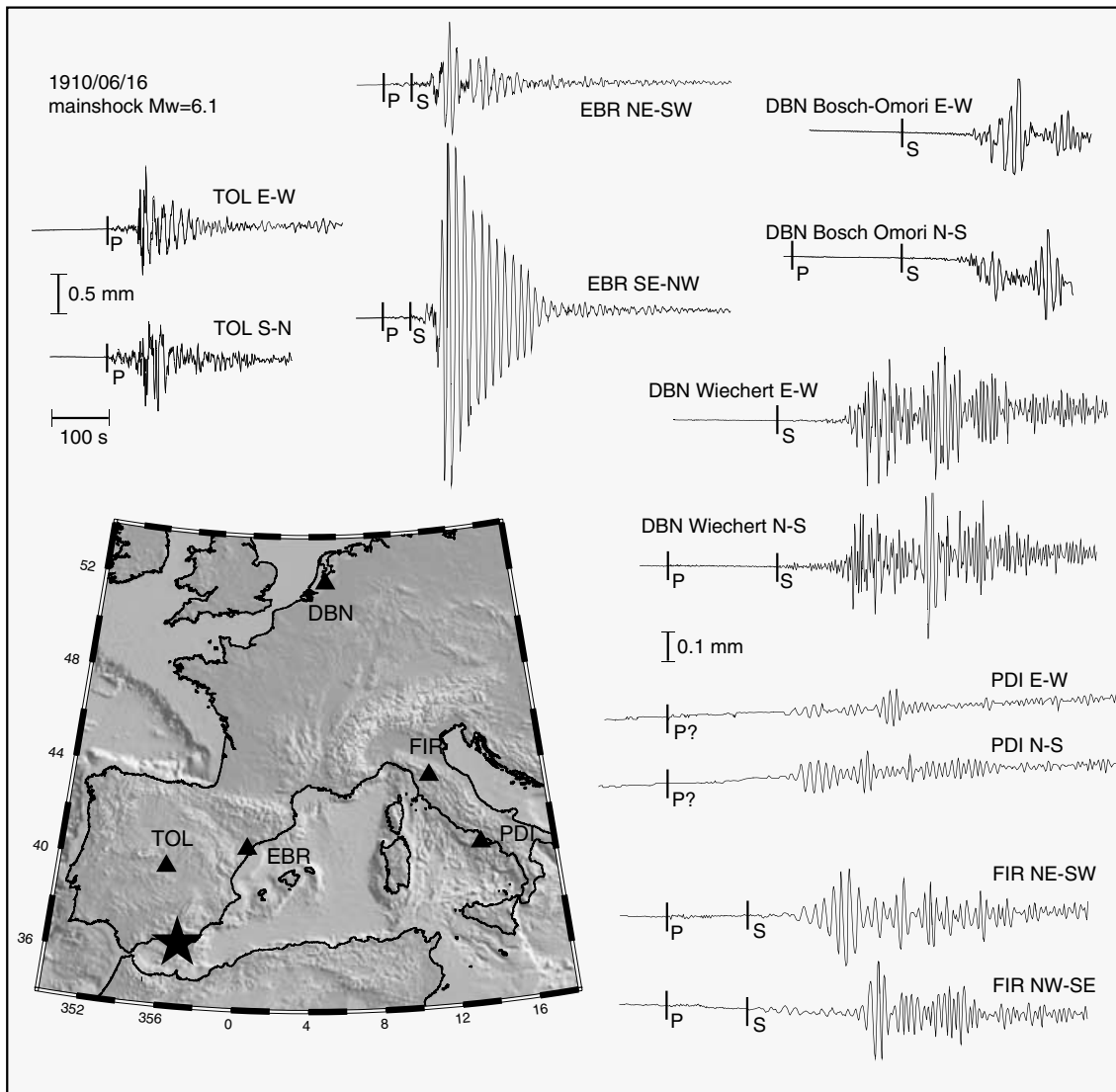

Figure 1. Historical recordings of the 1910 Adra earthquake from six two-component horizontal instruments at five observatories in Spain, Italy and the Netherlands. Traces have been corrected for curvature and amplification. The horizontal bar marks 100 s, the vertical bars mark 0.5 mm (TOL, EBR) and 0.1 mm (DBN, PDI, FIR). The map shows the recording geometry.

Table 1. Instrument characteristics and recording geometry for the historical seismographs used in this study. The zeros of the transfer functions are the same for all instruments (two zeros at the origin). Distance and azimuth are given relative to the epicentre of Vidal (1986).

	Instrument	Components	$T_0(s)$	Damping	Magnitude	Poles	Distance (km)	Azimuth
TOL	Bosch-Omori	S–N	17.0	0.4	13.1	$-0.148 \pm i0.339$	375	347.4°
		E–W		0.3	15.6	$-0.111 \pm i0.353$		
EBR	Grablovitz	NE–SW/SE–NW	13.0	0.4	8	$-0.193 \pm i0.443$	564	32.2°
FIR	Stiattesi	NW–SE/NE–SW	18.0	0.3	25	$-0.105 \pm i0.333$	1456	52.3°
PDI	Grablovitz	N–S?	10.3	0.3	8	$-0.183 \pm i0.582$	1545	67.5°
		E–W?	14.3			$-0.132 \pm i0.419$		
DBN	Bosch-Omori	N–S/E–W	18.0	0.4	20	$-0.140 \pm i0.320$	1843	18.1°
DBN	Wiechert	N–S	6.0	0.45	180	$-0.471 \pm i0.935$	1843	18.1°
		E–W			160			

The recording instruments were purely mechanical sensors, that are characterized by their amplification, free period and damping. Free periods of these instruments are between 6 and 20 s, and damping around 0.4 (Table 1). For TOL and EBR, the contemporaneous bulletin data on instrument characteristics and polarities were double-checked *in situ* and tested using the original instruments. The individual instrument characteristics were processed to pole and zero type transfer functions (for example Batlló & Bormann 2000) and then deconvolved from the recordings to obtain ground displacement seismograms. At each station, the two components were aligned at a common reference time, which were usually synchronous time marks on the seismograms. The only exception is TOL, where the time registration for both traces worked independently and should not be expected to be synchronized correctly. Toledo traces were aligned at the clear and coherent *P* arrival. Then traces were rotated to separate radial and transverse components. Prior to rotation, a 2-s lowpass filter was applied to minimize distortion by small misalignments due to picking inaccuracy and parallax problems at time mark generation.

One goal was to perform a regional moment tensor inversion for the Adra mainshock, using a time domain technique that incorporates information from the complete waveforms. The period band which we will use (20 to 50 s) is below the flat part of the instrument response, where sensor sensitivity quickly decreases, and we had to confirm whether the 1910 Adra mainshock radiated sufficient long period energy to generate high quality signals on the records of the available instruments. Further we require accurate correction of instrument characteristics (polarities), as well as the absence of disturbances such as shifts or varying trends in the original recordings that may have been caused by instrument failures. Early instruments do not guarantee these high quality standards and before performing the inversion we examine the recordings one by one to evaluate their suitability and assign them appropriate weighting factors.

(1) TOL: The recordings are of good quality and valuable for inversion. The noise level is very low. Further, for the Toledo station as well as its successor PAB, our experience from regional moment tensor inversion indicates that a simple layered earth model permits very accurate modelling of observed waveforms from events in the Alboran Sea (Stich *et al.* 2003).

(2) EBR: The traces are of high quality and valuable for inversion. The noise level is very low. The transverse component, however, shows Love wave resonance, which we attribute to local structure (Vila *et al.* 1996) and cannot expect to match with a regional earth model.

(3) DBN: The recordings of the Bosch-Omori seismograph are severely distorted by trends and were discarded for moment tensor inversion. The recordings of the Wiechert seismograph are of good quality for the *P* and *S* waves, but show several offsets during the surface wave recordings, the first possibly 350 s after the *P* arrival. After correction and filtering, these offsets distort the surface waveforms, so seismograms were cut before these offsets. The surface wave amplitudes are very large, suggesting site effects in the sedimentary environment.

(4) PDI: Data quality is poor. The traces show several smaller shifts. *P* and *S* waves are not well resolved and arrival times are uncertain. The polarities are unverified. The entire traces have low signal in the long period band. This station will be given a zero weight in inversion, but we will compute synthetic seismograms for the inverted moment tensor to confirm a basic compatibility with the observed surface wave amplitudes.

(5) FIR: Short period *P* and *S* waves are clearly recorded at this station, but their amplitudes are small and their signal-to-noise ratio in the long period band is insufficient for time domain inversion. At the surface wave arrival, the NW–SE component apparently failed to reproduce ground motion correctly: The large amplitude arrivals start almost 2 min late. This leads to a distortion of the rotated surface waves, especially for the transverse component nearly parallel to the NW–SE sensor. Like PDI, FIR will be given a zero weight in inversion.

MOMENT TENSOR INVERSION

We inverted for the best deviatoric moment tensor solution by minimizing the least-squares misfit between observed displacement seismograms within a long period passband (20 to 50 s) and their synthetic predictions corresponding to the moment tensor. The synthetic displacements are given by a linear combination of 5 independent moment tensor elements and a set of elementary Green's functions (Langston *et al.* 1982). Green's functions were computed with a reflectivity algorithm for a layered halfspace (Kennett 1983; Randall 1994). For the stations TOL, EBR and DBN with predominantly continental travelpaths the underlying lithospheric model approximates average continental (Hercynian) conditions (Table 2). For the Italian stations FIR and PDI with predominantly off shore propagation paths a western Mediterranean Sea model was used. These earth models have previously been shown to be appropriate for modelling long period waveforms for events throughout the Ibero-Maghrebian region (Stich *et al.* 2003). The point source Green's functions were convolved with a 4.5 s wide unit-area trapezoidal source time function according to the results of aftershock deconvolution, which will be discussed in the next section. The epicentre location was set at latitude 36.58° North, longitude 3.08° West (Vidal 1986), and the hypocentre depth was left open as it is poorly constrained and has major influence on the Green's function characteristics. Green's

Table 2. Regional layered earth models used for Green's function computation. The Western Mediterranean model is used for predominantly offshore travelpaths (FIR, PDI) and the Hercynian model for predominantly continental travelpaths (TOL, EBR, DBN). Layer thickness Δz is given in km, propagation velocities Vp and Vs in km s^{-1} and density in g cm^{-3}.

Western mediterranean				Hercynian model			
Δz	v_P	v_S	ρ	Δz	v_P	v_S	ρ
3	4.80	2.76	2.40	2	5.40	3.10	2.50
9	6.10	3.52	2.75	12	6.10	3.51	2.75
9	6.50	3.74	2.85	12	6.40	3.68	2.85
25	7.90	4.45	3.30	6	6.90	3.94	2.90
100	7.90	4.30	3.35	50	8.10	4.60	3.30
∞	8.20	4.70	3.40	100	8.10	4.40	3.35
				∞	8.20	4.70	3.40

functions were calculated for 15 equally spaced depths from 2 to 30 km which were tried successively to find the best combination of mechanism and depth.

Traces and synthetics were aligned at the *P* arrival except for station DBN, where traces were aligned at the arrival of the *S* waves, which we primarily want to match at that station. In accordance with the above mentioned data characteristics, FIR and PDI have zero weight. The inversion is based on the stations TOL, EBR and DBN, the individual traces are weighted to balance the different amplitudes and improve the overall fit of the waveforms (Fig. 2). For the radial components at TOL and EBR, the small amplitude *P* waves and the large amplitude Rayleigh-wave portion are weighted independently. For the parameters selected, the best solution fits 69 per cent of the observed waveforms. It indicates oblique strike slip faulting and a seismic moment of $M_0 = 1.50 \cdot 10^{18}$ Nm, moment magnitude $M_W = 6.1$. The double couple component has a right-lateral nodal plane $122°/80°/-137°$ and a left-lateral nodal plane $23°/48°/-13°$ (values for strike/dip/rake respectively, Aki & Richards 2002). The non-double-couple component is small (9 per cent) indicating that,

at long periods, this earthquake can be adequately modelled as a simple faulting event. The best solution is obtained at a depth of 16 km, slightly deeper than expected in this area. The inverted depth is model sensitive and the average continental velocity model does not match local crustal structure at the epicentre (for example Banda *et al.* 1993). In any case neither total misfit nor the focal mechanism change significantly between 12 and 22 km depth, indicating that the depth resolution of the inversion is low, but the inverted mechanism is stable.

Waveform matches between the corresponding predictions and the observations are good at TOL (Fig. 2). Also at EBR the similarity is high. The *P* waves are matched well and the Rayleigh wave prediction matches the amplitudes, but slightly mismatches the phase. We attribute this to complex crustal structure along the wave path at the eastern coast of Spain. The transverse component at EBR is well matched until the beginning of Love-wave resonance. For the Italian station, FIR and PDI (excluded from inversion), the observed amplitudes of body and surface waves are broadly consistent with the radiation pattern of the computed moment tensor, except for the transverse component of FIR which is affected by instrumental problems in the NW–SE component. At DBN, the near nodal *P* waves and the long period *S* waves are predicted correctly until we cut the traces short before instrument failures in the surface wave recordings.

The recording geometry of the 1910 Adra earthquake is certainly unfavourable for moment tensor inversion; the contributing stations cover only 45° of azimuthal interval between TOL and EBR. Regardless of the good waveform matches, this raises the question of whether the source mechanism is well constrained by the data or whether a great variety of source mechanisms are consistent with the available observations. We address this question by forward modelling waveforms of alternative mechanisms, and comparing them with the observations by means of their least-squares misfits. Neglecting the small non-double-couple component, we assume a pure
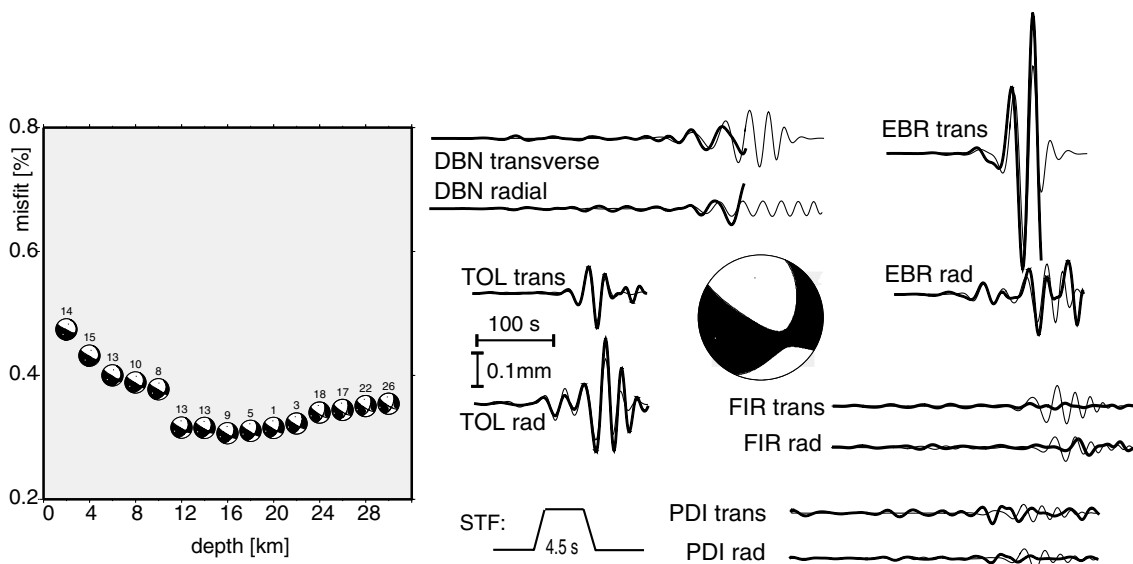

Figure 2. Best fitting moment tensor solution, corresponding to oblique strike slip faulting at 16 km depth, in lower-hemisphere, equal-area projection. The total misfit is 31 per cent, the CLVD component 9 per cent. The inverted mechanisms and misfits for other depths are shown for comparison in the diagram (small numbers next to the mechanisms indicate the percentage of CLVD component). Prior to inversion, synthetics were convolved with the 4.5 s trapezoidal source time function. The individual waveform matches for the best solution are illustrated by overlaying observed (thick lines) and predicted (thin lines) long period waveforms. The vertical bar corresponds to 0.1 mm displacement, the horizontal bar to 100 s. All traces start 100 s before the *P* arrival. Observed seismograms were cut where instrumental failures (DBN) or receiver site resonance phenomena (EBR Love-waves) affected the waveforms.
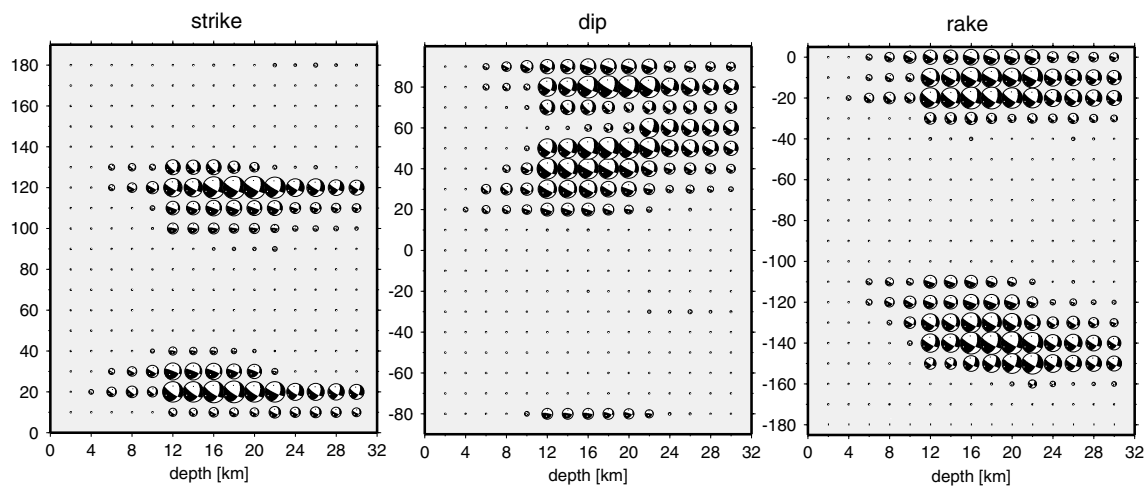
Figure 3. Best grid-search solutions for each depth vs strike, dip and rake. The sizes of the mechanisms have been scaled linearly with the fractional fit to the observed waveforms between 53 per cent (scale = 0) and 68 per cent (scale = 1). These resolution tests indicate well-constrained estimates for both strike values (±10°), as well as for the 80° dip.

faulting solution. Then we can perform a complete search for alternative mechanisms in a 4-D grid over hypocentral depth, strike, dip and rake (Stich *et al.* 2003). Grid spacing is 2 km for depths between 2 and 30 km, and 10° for the entire range of fault plane parameters. The best grid search result has strike 120°, dip 80°, rake −140°, depth 18 km, and fits 68 per cent of the waveforms, very similar to the moment tensor solution. On the basis of previous experience, we consider possible all those alternative mechanisms that correspond to fits better than 10 per cent below the reference level of the best grid search result. That means they have to reproduce at least 58 per cent of the observed waveforms for the Adra earthquake. Alternative faulting solutions are shown in three fault-parameter vs depth diagrams (Fig. 3).

As in inversion, the best solutions for the double couple grid search are obtained between 12 and 22 km depth. The strike value for both nodal planes and the dip value of the N120°E plane are well resolved (±10°). The second dip value is less certain, which we already observed during moment tensor inversion where this dip showed sensitivity to variations of the weighting factors. This ambiguity is propagated to the resolution of rake, leading to a ±20° error for the rake of the N120°E plane. Consequently, we cannot specify the ratio of strike-slip to dip-slip exactly. Positive rakes were clipped in the figure, as they were observed only for a vertical nodal plane where rake can reverse the sign. For non-vertical planes, the resolution test excludes reverse faulting components. In conclusion, the available narrow-azimuth data constrain the source mechanism well, especially the 80° dipping N120°E nodal plane. We attribute this outcome to the fact that this nodal plane lies between the high quality stations TOL and EBR.

AFTERSHOCK DATA

Recordings of the major aftershock are available from TOL, EBR and both Wiechert and Bosch-Omori instruments at DBN. They were processed in the same way as the mainshock data. For this event, the available data do not permit a regional moment-tensor inversion. A major drawback is the distortion by offsets and trends in the S–N component at the nearest station TOL, making this important station useless. Ground motion at EBR and the Wiechert instrument at DBN seem to be properly recorded, but the resolution of the body

waves is low, on account of the small amplification factor and the long distance respectively. Surface waves at these stations are well recorded in the short period band, but the signal-to-noise ratio at long periods is low. Recordings at the Bosch-Omori seismograph at DBN are severely distorted (Fig. 4).

The available waveforms show striking similarity to the corresponding mainshock recordings. This indicates similar radiation patterns for both earthquakes and similar orientation of source mechanisms. Assuming that path and radiation effects are essentially the same for both events, we deconvolve the aftershock recordings from the main event to estimate the relative source time function of the earthquakes. We should be aware of two limitations: The small azimuthal coverage cannot resolve the directivity effect of lateral rupture propagation. The aftershock is of moderate to large size and not a delta function response to the path effects. Its rupture history may be non-uniform, since seismotectonic structures in the source area are known to be small-scale (≈1 km), and complex source time functions have been found for $M_W \approx 5$ events (Stich *et al.* 2001). Deconvolution was performed with an iterative time-domain technique that sums Gaussian pulses into the deconvolved function until no more significant changes occur (Ligorría & Ammon 1999; Kikuchi & Kanamori 1982). A Gaussian pulse width of 2 Hz was chosen, which roughly corresponds to a 1 Hz lowpass filter for the relative source time function. This helps to smooth out the effects of noise and non-uniform aftershock rupture. Deconvolutions were calculated both for body and surface wave windows and both for original recordings and corrected displacement recordings. This allows averaging out noise by stacking up to eight time functions for each station. Deconvolutions at TOL S–N component show ringing, probably on account of the data insufficiencies described above, and were discarded. DBN had also to be discarded, probably because noise in the aftershock recordings reduces the similarity among the waveforms. The remaining deconvolutions correspond to good fits between observed and predicted mainshock seismograms, supporting the use of the aftershock for path calibration.

We show stacked relative source time functions at TOL and EBR, an average stack for both stations, and a selected stack for both stations that includes only deconvolutions which reproduce at least 80 per cent of the observed seismograms (Fig. 5). The time
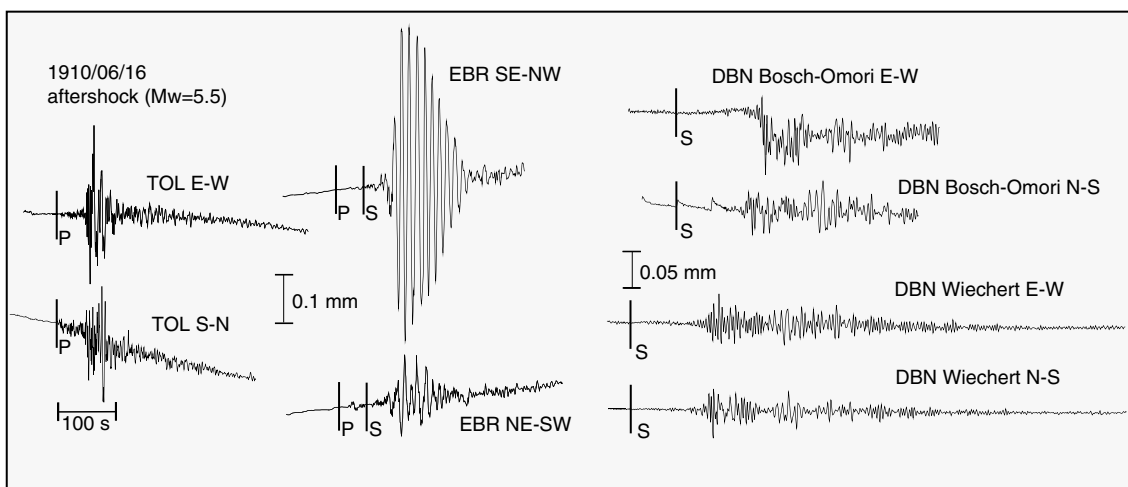
Figure 4. Historical recordings of the major aftershock on 1910 June 16 at four instruments. Traces are corrected for curvature and amplification. The horizontal bar marks 100 s, the vertical bars 0.1 mm (TOL, EBR) and 0.05 mm (DBN).
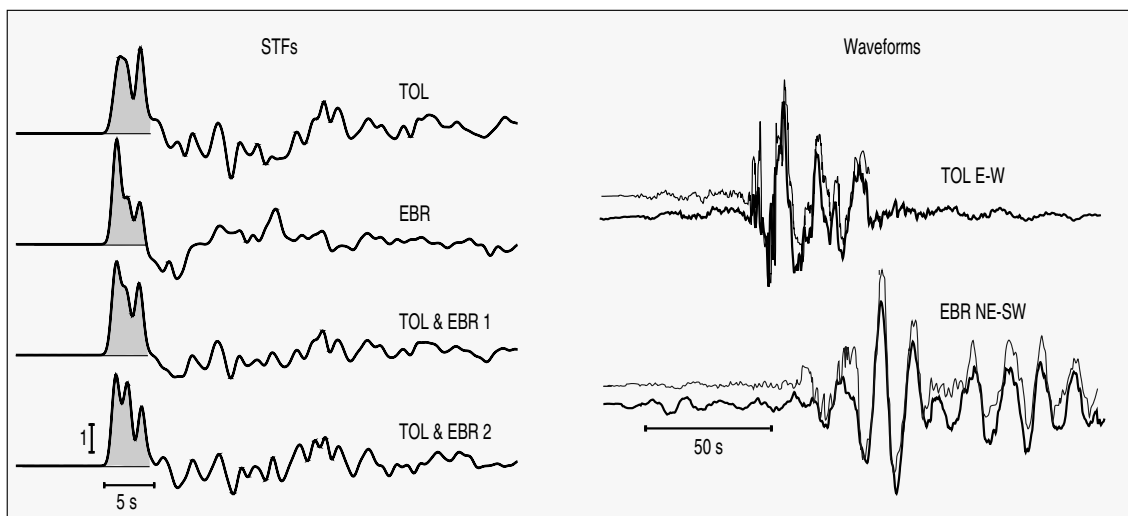

Figure 5. Left: Relative source time function of the 1910 Adra earthquake as obtained by deconvolving the major aftershock. From top to bottom, the figures show the relative time functions from a stack of deconvolved functions at TOL; deconvolved functions at EBR; an average stack at both stations (TOL and EBR 1); and at both stations with quality threshold (deconvolved functions reproduce more than 80 per cent of the initial seismograms, TOL and EBR 2). The relative time function has an overall trapezoidal shape and a total duration of 4 s. Right: Examples of fit between observed mainshock waveforms (thin lines) and predicted waveforms (convolution of relative source time function and aftershock waveform, thick lines) at TOL and EBR.

functions have a total duration of about 4 s, an overall trapezoidal shape and sharp risetimes of about 1 s. Despite the low pass filter, three consecutive episodes of major moment release can be identified, indicating a sequence of subevents. The first and second subevents together constitute about 75 per cent of the total moment release. Differing relative amplitudes at TOL and EBR for the third subevent might be caused by different source depth or faulting orientation. The small non-double-couple component of the composite moment tensor suggests some similarity among the focal mechanisms of the subevents, such as (sub-)parallel fault planes or slip vectors (Julian *et al.* 1998). The integral over the relative source function indicates the ratio between the seismic moments of the mainshock and the aftershock (Mori & Frankel 1990). Since the deconvolution reproduces typically only 70 to 90 per cent of the mainshock seismogram power, the initial ratios tend to be underpredicted and were normalized using the scale factor between observed and predicted mainshock seismograms. After this correction, we obtain ratios of about 8 between the two moments, corresponding to $M_0 = 1.9 \cdot 10^{17}$ Nm and $M_W = 5.5$ for the aftershock.

To convert the relative source time function to an estimated absolute time function for the main event, we convolved a generic source time function for the magnitude 5.5 event. A triangle with total duration of 1.5 s was chosen, as that has shown to be appropriate for crustal magnitude 5.5 events elsewhere (Singh *et al.* 2000). The convolution does not broaden the source time function significantly, giving an estimate of 4.5 s for the total rupture duration. This leads to an estimate for the total rupture length of 12 km, assuming unilateral rupture propagation at an average velocity of 0.8 times the shear velocity $Vs = 3.4$ km s^{-1} (Serrano 1999). The estimated dynamic stress drop corresponding to a total moment release of $1.50 \cdot 10^{18}$ Nm is 29 bar (Brune 1970). However, the lack of knowledge of the true rupture pattern and directivity effects introduces considerable uncertainties into the estimates for rupture length and stress drop.

TECTONIC INTERPRETATION

The 1910 earthquake occurred near the northern edge of the Alboran Sea basin. Despite its location on the convergent African–Eurasian plate boundary, the Alboran Basin underwent significant crustal extension (Banda *et al.* 1993), approximately from the early Miocene on (for example Docherty & Banda 1995). The process of basin extension in a convergent environment is commonly attributed to removal of upper mantle lithosphere (Calvert *et al.* 2000; Seber *et al.* 1996; Morales *et al.* 1999; Gutscher *et al.* 2002). Focal mechanism data indicate a nearly east–west orientation of present-day extension (Mezcua & Rueda 1997; Stich *et al.* 2003). The 1910 mainshock was responsible for about 60 per cent of the total moment release in the north-eastern Alboran basin over the last 100 yr (ISC, International Seismological Centre, On-line Bulletin, http://www.isc.ac.uk/Bull) and its source mechanism should well reflect the average regional stress conditions. The moment tensor solution strongly resembles recent small to moderate events in the region, showing strike-slip to oblique normal faulting style, nearly N–S oriented *P* axes ($\approx$N350°E) and nearly E–W oriented *T* axes ($\approx$N80°E, Fig. 6). The *P*-axis orientation for the Adra 1910 earthquake is N352°E at plunge 36° and the *T*-axes orientation is N245°E at plunge 21°. The corresponding deformation is similar to the neotectonic deformation observed onshore around Adra, controlled by approximately ENE–WSW extension (Rodriguez-Fernandez & Martin-Penela 1993). We believe that this consistency also supports the inverted moment tensor solution for the Adra earthquake.

According to the aftershock deconvolution, the 1910 Adra earthquake ruptured more than 10 km of crust and must be related to a major fault. In the offshore setting, however, no major tectonic structure has been mapped that can be clearly associated with the earthquake. Industrial seismic reflection profiles in the Alboran Sea show faults (Rodriguez-Fernandez & Martin-Penela 1993), but their orientation and extension is uncertain. Besides, the possibly large epicentral errors of the 1910 events hamper a proper assignment. To determine which of the nodal planes of the mechanism was most likely to be the active fault plane, we take into consideration the pattern of neogene faults in nearby onshore areas. The faults with major recent displacement are steeply dipping N120°E to N130°E faults, while other dominant fault directions between N70°E and N90°E were developed in the Messinian and Pliocene stress field and show little evidence of activity under recent stress conditions (Rodriguez-Fernandez & Martin-Penela 1993). The orientation of offshore seismogenic structures in the source area of the 1910 Adra event has been investigated by precise relocations within the seismic series following the moderate M_w 4.8 and 4.9 Adra earthquakes of 1993 and 1994 (Stich *et al.* 2001 Fig. 6). Cluster relative locations reveal a clear predominance of N120°E to N130°E oriented faults and few N60°E to N70°E structures, where the latter are possibly of Pliocene origin and reactivated in the current stress field as oversteps for N120–130°E faults. Correlating these neo- and seismotectonic data with the moment tensor solution, we find no neotectonic equivalent for the N23°E plane, but clear evidence for N120–130°E striking, steeply dipping faults near the event location.
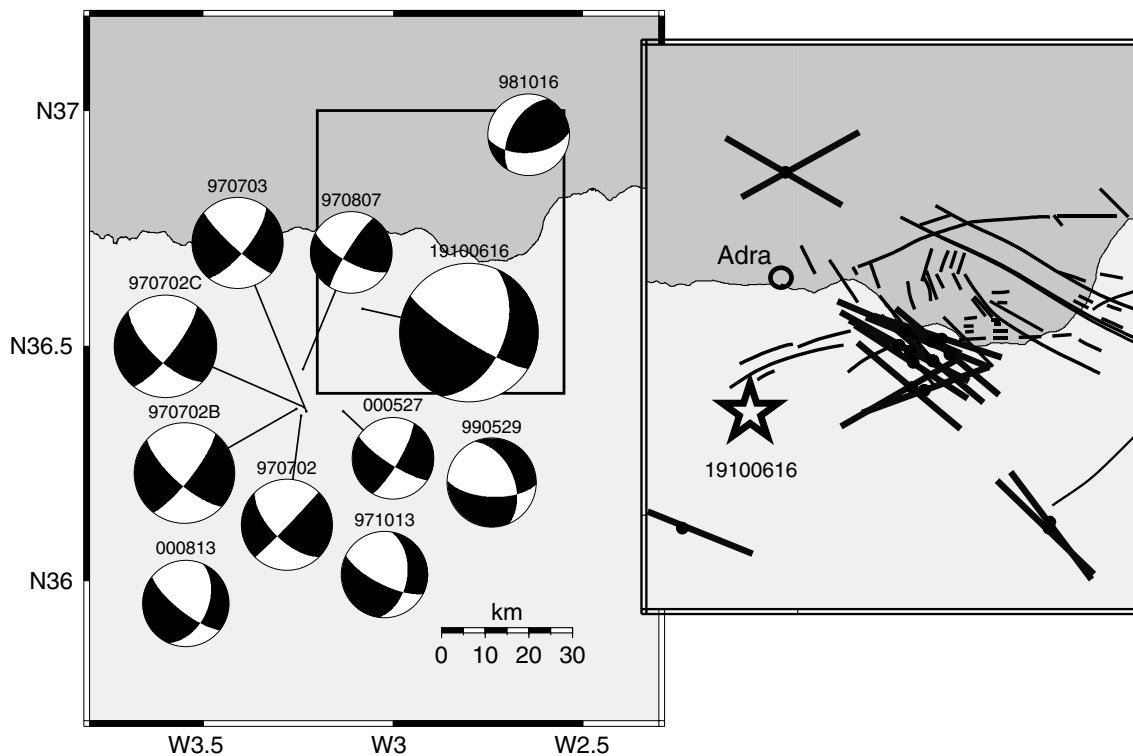

Figure 6. Correlation of the mainshock mechanism with local tectonic data. Left map: Comparison of faulting solutions from regional moment tensor inversion of small to moderate events (M_w = 3.6 to 4.5) in the northeastern Alboran Basin (Stich *et al.* 2003), and for the 1910 Adra earthquake. Right map: Strike directions of Neogene faults (thin lines, redrawn from Rodriguez-Fernandez & Martin-Penela 1995) and seismogenic structures (thick lines, obtained from relative locations of multiplet events, Stich *et al.* 2001) in the epicentral area. These data clearly support the conclusion that the N122°E nodal plane was the active fault plane.

CONCLUSIONS

We inverted the moment tensor of the $M_W = 6.1$, 1910 Adra mainshock, based on three out of six available recordings at mechanical horizontal seismographs in Spain, Italy and the Netherlands. The moment tensor solution corresponds to a 91 per cent double-couple with strike-slip-to-normal faulting style. Considering available information on local seismotectonics, our preferred faulting solution for the 1910 Adra earthquake is striking 122°, dipping 80°, and has a rake of −137°. Despite considerable deficits in data quality and station coverage, grid search modelling of faulting solutions indicates that available data are able to constrain the source mechanisms and these sparse, early 20th century records represent a valuable resource for modelling the source mechanism of a large regional earthquake. The capture of a major, $M_W = 5.5$ aftershock by the same network permits the deconvolution of a relative source time function for the 1910 mainshock: The observed rupture duration and the inferred rupture dimension show values typical of an earthquake of this magnitude, and consequently also the stress drop estimate is typical of interplate events.

This study provides seismotectonic information on a large, historic earthquake in the Alboran Basin at the African–Eurasian plate boundary. The mechanism of the 1910 earthquake is consistent with moment tensors of nine nearby small to moderate events that have occurred since 1997. Both the recent events with an accumulated moment release of $1.53 \cdot 10^{16}$ Nm and the 1910 earthquake with a moment release almost 100 times larger, respond te same stress conditions. The historical earthquake confirms a strike-slip-to-normal faulting style and an E–W to ENE–WSW direction of extension in the Alboran Basin. The preferred faulting solution for the 1910 Adra earthquake indicates a potential for a set of parallel N120°–130°E faults along the northern edge of the Alboran Basin to generate destructive earthquakes.

ACKNOWLEDGMENTS

REFERENCES

Aki, K. & Richards, P.G., 2002. *Quantitative Seismology: Theory and Methods*, 2nd edn, University Science Books, Herndon.

Banda, E., Gallart, J., García-Dueñas, V., Dañobeitia, J.J. & Makris, J., 1993. Lateral variations of the crust in the Iberian Peninsula, New evidence from the Betic Cordillera, *Tectonophysics,* **221,** 53–66.

Batlló, J. & Bormann, P., 2000. A catalog of Old Spanish Seismographs, *Seism. Res. Lett.,* **71,** 570–582.

Batlló, J., Susagna, T. & Roca A., 1997. A processing system for old records of regional earthquakes: analysis of the 19 November 1923 earthquake in the Pyrenees, *Cahiers du Centre Européen de Géodynamique et de Séismologie,* **13,** 159–175.

Brune, J.N., 1970. Tectonic stress and the spectra of seismic shear waves from earthquakes, *J. geophys. Res.,* **75,** 4997–5009.

Calvert, A. *et al.* 2000., Geodynamic evolution of the lithosphere and upper mantle beneath the Alboran region of the western Mediterranean: Constraints from traveltime tomography, *J. geophys. Res.,* **105,** 10 871–10 898.

Chung, W. & Kanamori, H., 1976. Source process and tectonic implications of the Spanish deep-focus earthquake of March 29, 1954, *Phys. Earth planet. Int.,* **13,** 85–96.

Dineva, S., Batlló, J., Mihailov, D. & van Eek, T., 2002. Source paramenters of four strong earthquakes in Bulgaria and Portugal at the beginning of the 20th century, *J. Seism.,* **6,** 99–123.

Docherty, C. & Banda, E., 1995. Evidence for the eastward migration of the Alboran Sea based on regional subsidence analysis: A case for basin formation by delamination of the subcrustal lithosphere?, *Tectonics,* **14,** 804–818.

Grabrovec, D. & Allegretti, I., 1994. On the digitizing of historical seismograms, *Geofizika,* **11,** 27–31.

Gutenberg, B. & Richter, C.F., 1954. *Seismicity of the Earth and Associated Phenomena*, Princeton University Press, Princeton.

Gutscher, M.A., Malod, J., Rehault, J.P., Contrucci, I., Klingelhoefer, F., Mendes-Victor, L. & Spakman, W., 2002. Evidence for active subduction beneath Gibraltar, *Geology,* **30,** 1071–1074.

Julian, B.R., Miller, A.D. & Foulger, G.R., 1998. Non-Double-Couple Earthquakes; 1. Theory, *Rev. Geophys.,* **36,** 525–549.

Karnik, V., 1969. *Seismicity of the European Area*, Part 1, Reidel, Dordrecht.

Kennett, B.L.N., 1983. *Seismic wave propagation in stratified media*, Cambridge University Press, Cambridge.

Kikuchi, M. & Kanamori, H., 1982. Inversion of complex body waves, *Bull. seism. Soc. Am.,* **72,** 491–506.

Langston, C.A., Barker, J.S. & Pavlin, G.B., 1982. Point-source inversion techniques, *Phys. Earth planet. Int.,* **30,** 228–241.

Ligorría, J.P. & Ammon, C.J., 1999. Iterative Deconvolution and Receiver-Function Estimation, *Bull. seism. Soc. Am.,* **89,** 1395–1400.

Mezcua, J. & Rueda, J., 1997. Seismological evidence for a delamination process in the lithosphere under the Alboran Sea, *Geophys. J. Int.,* **129,** 1–8.

Morales, J., Serrano, I., Jabaloy, A., Galindo-Zaldivar, J., Zhao, D., Torcal, F., Vidal, F. & Gonzalez-Lodeiro, F., 1999. Active continental subduction beneath the Betic Cordillera and Alboran Sea, *Geology,* **27,** 735–738.

Mori, J. & Frankel, A., 1990. Source parameters for small events associated with the 1986 North Palm Springs, California, earthquake determined using empirical Green functions, *Bull. seism. Soc. Am.,* **80,** 278–295.

Randall, G.E., 1994. Efficient calculation of complete differential seismograms for laterally homogeneous earth models, *Geophys. J. Int.,* **118,** 245–254.

Rodriguez-Fernandez, J. & Martin-Penela, A.J., 1993. Neogene evolution of the Campo de Dalías and the surrounding offshore areas (Northeastern Alboran Sea), *Geodinamica Acta,* **6,** 255–270.

Samardjieva, E., Payo, G. & Lopez, C., 1997. Old regional seismograms at the Toledo observatory. Their study by computer techniques, *Cahiers du Centre Europeen de Geoynamique et de Seismologie,* **13,** 159–175.

Sanchez Navarro-Neumann, M., 1911. Los recientes terremotos granadinos (Mayo-Junio de 1911), *Rev. Soc. Astr. de Esp. y Amer.,* 53–56.

Seber, D., Barazangi, M., Ibenbrahim, A. & Demnati, A., 1996. Geophysical evidence for lithospheric delamination beneath the Alboran Sea and Rif-Betic mountains, *Nature,* **379,** 785–790.

Serrano, I., 1999. Distribución espacial de la sísmicidad en las Cordilleras Béticas-Mar de Alborán, *PhD thesis*, University of Granada, Granada.

Singh, S.K., Pacheco, J., Ordaz, M., & Kostoglodov, V., 2000. Source Time Function and Duration of Mexican Earthquakes, *Bull. seism. Soc. Am.,* **90,** 468–482.

Stich, D., Alguacíl, G. & Morales, J., 2001. The relative location of multiplets in the vicinity of the Western Almería (southern Spain) earthquake series of 1993–1994, *Geophys. J. Int.,* **146,** 801–812.

Stich, D., Ammon, C.J. & Morales, J., 2003. Moment tensor solutions for small and moderate earthquakes in the Ibero-Maghreb region, *J. geophys. Res.* **108,** 2002JB002057.

Vidal, F., 1986. Sismotectónica de la región Beticas- Mar de Alborán, *PhD thesis*, University of Granada, Granada.

Vila, J., Batlló, J. & Correig, A. M., 1996. Lateral variations of the local magnitude at Ebro station, North Eastern Iberian Peninsula, *Pageoph,* **147,** 131–146.